

# Generation of Terahertz Radiation by Optical Excitation of Aligned Carbon Nanotubes

Lyubov V. Titova,<sup>†,‡</sup> Cary L. Pint,<sup>§</sup> Qi Zhang,<sup>⊥,¶</sup> Robert H. Hauge,<sup>||</sup> Junichiro Kono,<sup>⊥,¶</sup> and Frank A. Hegmann<sup>†</sup>

<sup>†</sup>Department of Physics, University of Alberta, Edmonton, Alberta T6G 2E1, Canada

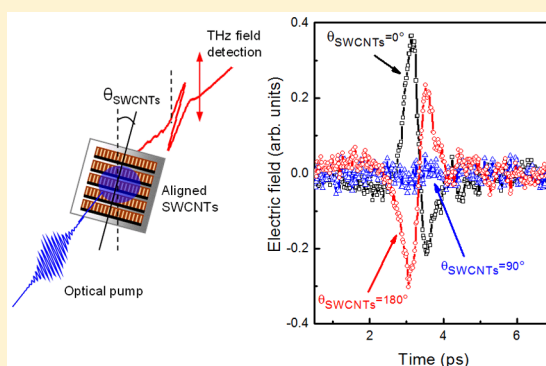
<sup>‡</sup>Department of Physics, Worcester Polytechnic Institute, Worcester, Massachusetts 01609, United States

<sup>§</sup>Department of Mechanical Engineering, Vanderbilt University, Nashville, Tennessee 37240, United States

<sup>⊥</sup>Department of Electrical and Computer Engineering, <sup>¶</sup>Department of Physics and Astronomy, and <sup>||</sup>Department of Chemistry, Rice University, Houston, Texas 77005, United States

**S** Supporting Information

**ABSTRACT:** We have generated coherent pulses of terahertz radiation from macroscopic arrays of aligned single-wall carbon nanotubes (SWCNTs) excited by femtosecond optical pulses without externally applied bias. The generated terahertz radiation is polarized along the SWCNT alignment direction. We propose that top-bottom asymmetry in the SWCNT arrays produces a built-in electric field in semiconducting SWCNTs, which enables generation of polarized terahertz radiation by a transient photocurrent surge directed along the nanotube axis.



**KEYWORDS:** Single-wall carbon nanotubes, SWCNTs, terahertz generation, THz pulses

In recent years, unique electronic and optical properties of carbon-based nanomaterials such as single-wall carbon nanotubes (SWCNTs) and graphene have made them attractive candidates for developing next-generation photonic and optoelectronic devices.<sup>1–6</sup> In particular, SWCNTs are emerging as the material of choice for devices working in the terahertz (THz) range where conventional solid-state technology is yet to provide effective solutions.<sup>7</sup> Nearly ideal, broadband THz polarizers and powerless, polarization sensitive THz detectors based on aligned carbon nanotube films have already been demonstrated.<sup>8,9</sup> An unaligned semiconducting SWCNT film has been shown to act as an ultrafast THz polarization modulator.<sup>10</sup> Emission of broadband THz pulses due to excitation of ultrafast transient photon-drag currents has been observed in single-layer graphene, which exhibited significant enhancement due to coupling to surface plasmon modes in a gold substrate.<sup>11</sup> Theory also predicts that chiral SWCNTs can be used as frequency multipliers and metallic SWCNTs as emitters in the THz range.<sup>12,13</sup> The possibility of THz emission by metallic SWCNTs through heating of the electron gas and resulting population inversion in an applied electric field has also been explored theoretically.<sup>12,13</sup>

One method for generating free-space propagating, broadband THz pulses is by optical rectification of femtosecond-duration optical pulses in materials with a significant second-order susceptibility,  $\chi^{(2)}$ , such as inorganic semiconductors

ZnTe, LiNbO<sub>3</sub>,<sup>14–16</sup> organic semiconductors DAST, OH1, and others,<sup>17,18</sup> or poled polymers.<sup>19</sup> Another way of generating THz pulses involves excitation of a transient photocurrent by an ultrafast optical pulse. The photocurrent can be driven by an applied bias voltage such as in a photoconductive switch,<sup>14–16</sup> by intrinsic electric fields at semiconductor surfaces, or by differences in electron and hole mobilities (photo-Dember effect), resulting in transient charge separation upon excitation of a semiconductor surface.<sup>20,21</sup> Recently, generation of THz pulses in thermoelectric materials such as BiSnTe and BiTeSe by the fast diffusion of free majority carriers as a result of an ultrafast laser-induced temperature gradient (Seebeck effect) has also been observed.<sup>22</sup> THz emission with efficiencies surpassing that of bulk semiconductors has been reported in a variety of nanowires and nanorods.<sup>23–26</sup> In these experiments, dense, vertically aligned nanowire or nanorod arrays on growth substrates were excited by ultrafast optical pulses at off-normal incidence. Efficient THz generation in these structures was attributed to excitation of photocurrents driven by the intrinsic surface depletion field of the substrate, the photo-Dember field due to the difference in electron and hole mobilities, or by the

**Received:** February 5, 2015

**Revised:** March 28, 2015

**Published:** April 16, 2015

built-in contact field between a nanowire and a metal catalyst particle at its tip.<sup>23,25,26</sup> In carbon materials, generation of THz radiation by ultrafast optical pulses without an external bias was demonstrated in graphite<sup>27</sup> as well as in single-layer graphene.<sup>11</sup> In graphite, the emitted THz radiation was polarized along the *c*-axis of HOPG crystals, and its origin was tentatively ascribed to photoinduced transient currents in the built-in electric field created by accumulation of charges at stacking faults.<sup>27</sup> In graphene, on the other hand, THz generation has been attributed to the excitation of ultrafast transient photon drag currents.<sup>11</sup> THz generation in carbon nanotubes, however, has until now only been considered in theoretical investigations.<sup>12,13</sup>

Here, we report on THz generation from a macroscopically aligned SWCNT film without any externally applied voltage bias. We find that photoexcitation of an aligned SWCNT film with either 400 or 800 nm pulses results in emission of coherent, broadband THz pulses that are polarized along the SWCNT arrays and have a polarity that is determined by the array top-bottom anisotropy. We propose that this top-bottom asymmetry in the morphology of the aligned arrays creates a built-in electric field in the semiconducting SWCNTs, which enables efficient generation of THz radiation polarized along the axis of the nanotubes by a photocurrent surge following excitation with an optical pulse.

In our experiments, we used a highly aligned, 2- $\mu\text{m}$ -thick SWCNT film that was synthesized by water-assisted chemical vapor deposition, as described in detail in refs 28–32. Dense, vertically aligned rows of  $\sim 30\ \mu\text{m}$  long SWCNTs with a  $50\ \mu\text{m}$  pitch were grown using lithographically patterned catalyst substrates. The average diameter of the SWCNTs was  $\sim 2.7\ \text{nm}$ , and both metallic and semiconducting SWCNTs were present. Following growth, SWCNT rows were lifted from the catalyst-patterned substrate using high-temperature ( $750\ \text{°C}$ )  $\text{H}_2\text{O}$  vapor etching and were dry-transferred to a 1 mm thick *c*-cut sapphire substrate, as illustrated in Figure 1a. This process resulted in a film consisting of horizontally aligned SWCNT arrays. Optical microscopy (Figure 1b) and scanning electron microscopy (SEM, Figure 1c) images show excellent overall alignment in the resulting film. However, a significant amount of asymmetry still exists between the top and bottom ends of the SWCNT arrays both in alignment as well as the number density, as shown in Figure 1d,e. In the very top layer of nanotubes (Figure 1e) formed during nucleation, the SWCNT density is high, and the CNTs are straight with diameters of 1–5 nm, corresponding to the initial distribution of catalyst particle diameters.<sup>30,31</sup> Over the course of growth, catalyst nanoparticles undergo a process of Ostwald ripening where some particles disappear, thus terminating the growth of CNTs that originated on them. Meanwhile, others grow in size, resulting in a gradual increase in CNT diameters, a decrease in CNT density, and a marked decrease in CNT alignment close to the bottom of the array.<sup>30,31</sup>

The aligned SWCNT film on the sapphire substrate was excited at normal incidence with 400 or 800 nm, 100 fs laser pulses from a 1 kHz amplified Ti:sapphire source (Figure 2a). The optical pump beam size was  $\sim 5\ \text{mm}$  in diameter, resulting in excitation of many aligned SWCNTs simultaneously. The resulting THz pulses were coherently detected by free-space electro-optic sampling in a [110] ZnTe crystal.<sup>33</sup> The vertically polarized component of the generated THz pulses was detected, and the orientation of the sample (given by the angle  $\theta_{\text{SWCNT}}$ ) as well as the polarization of the optical pump

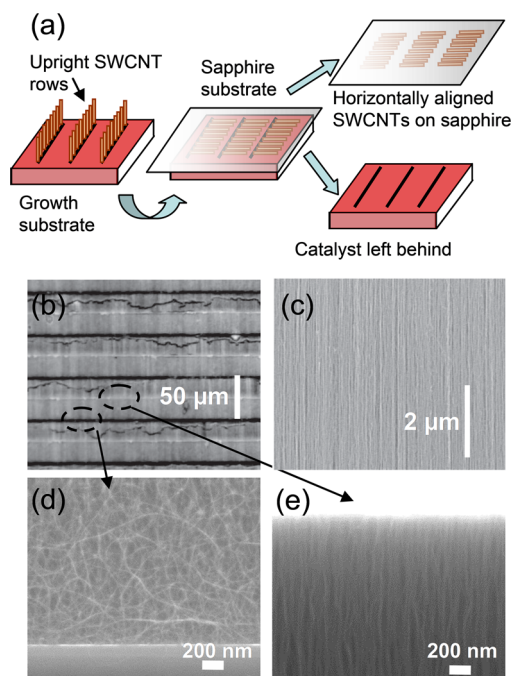


**Figure 1.** Aligned SWCNT film. (a) Schematic illustration of the dry contact transfer of aligned SWCNTs to a sapphire substrate. (b) Optical microscope image of the SWCNT film on a sapphire substrate showing arrays of highly aligned SWCNTs with uniform lengths and a pitch of  $50\ \mu\text{m}$ . (SWCNTs are aligned parallel to the scale bar.) (c) SEM image taken in the middle portion of a SWCNT array on a sapphire substrate showing the high degree of nanotube alignment. SEM images of the (d) bottom, corresponding to growth substrate side, and (e) top ends of a SWCNT array, showing a disordered, less dense array at the bottom and a highly aligned array at the top.

pulse (given by the angle of pump polarization relative to vertical,  $\theta_{\text{pump}}$ ) were varied, either by rotating the sample (former) or by using a half-wave plate (latter), as illustrated in Figure 2a.

An example of an emitted THz waveform in the time domain as well as its Fourier amplitude spectrum, generated by a horizontally polarized, 400 nm pump pulse with  $170\ \mu\text{J}/\text{cm}^2$  fluence and  $\theta_{\text{SWCNT}} = 0^\circ$ , are shown in Figure 2b. On the high frequency side, the observed bandwidth extends to  $>1.5\ \text{THz}$  and is not limited by the bandwidth of our detection system, 0.5–2.5 THz, as illustrated in Figure S1. Because of the suppressed response of the ZnTe detector crystal at low frequencies, we may, however, be underestimating how far the bandwidth of the generated THz pulses extends on the lower frequency side. We estimate that the THz generation efficiency of a 2  $\mu\text{m}$ -thick SWCNT film is  $6 \times 10^{-12}$  (see Supporting Information). We also established that the *c*-cut sapphire substrate does not contribute to THz generation, as no THz emission was found under the same excitation condition from the portions of the substrate not covered by the SWCNT film (Figure S2).

Figure 2c shows THz pulses emitted at different sample orientations and pump polarizations. Regardless of the pump polarization, the electric field of the emitted THz pulses is parallel to the SWCNTs, which suggests the existence of an ultrafast photocurrent surge along the SWCNTs. Furthermore, pump pulses polarized perpendicular to SWCNTs are significantly more efficient for THz generation. At first glance, this observation is counterintuitive given the known strong

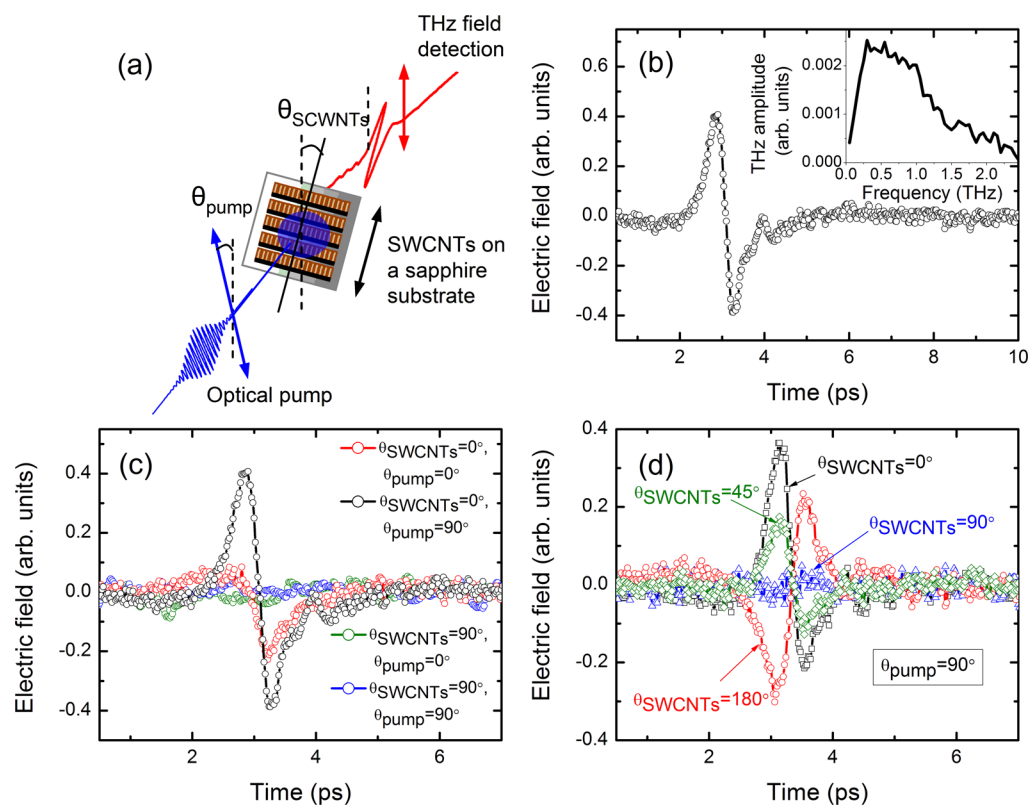


**Figure 2.** THz generation in the aligned SWCNT film: dependence on pump polarization and sample orientation. (a) Schematic illustration of the THz generation experiment. The SWCNTs are aligned vertically when  $\theta_{\text{SWCNTs}} = 0^\circ$ . (b) Example of a THz pulse emitted by the SWCNT film upon excitation with horizontally polarized pump pulses. (c) Emitted THz pulses for different pump polarizations and SWCNT film orientations. (d) Dependence of the emitted THz pulse amplitude and polarity on SWCNT film orientation, measured in a different spot on the sample compared to panel c, and with a horizontally polarized pump pulse. In panels b–d, the 400 nm, 100 fs optical pump pulses have an incident fluence of  $170 \mu\text{J}/\text{cm}^2$ .

anisotropy in optical absorption of carbon nanotubes that favors absorption of light polarized along the nanotube direction;<sup>10</sup> this point is discussed in detail later in this Letter.

Figure 2d illustrates the dependence of the amplitude and polarity of the emitted THz pulses on the SWCNT film orientation for optical pump polarization fixed along the horizontal direction ( $\theta_{\text{pump}} = 90^\circ$ ). Again, no THz emission is detected when the SWCNT alignment is normal to the THz detection direction. More importantly, the polarity of the THz pulse reverses while the amplitude and shape remain nearly unchanged when the film is rotated by  $180^\circ$ . The reversal of the THz pulse polarity upon rotation of the SWCNT arrays by  $180^\circ$ , also observed upon 800 nm excitation (Figure S3), suggests that the mechanism responsible for THz generation relies on top-bottom asymmetry in the properties of aligned SWCNTs arrays. One possible scenario involves THz generation by an ultrafast photocurrent surge driven by a built-in voltage in semiconducting SWCNTs present in the film. More targeted and spatially resolved measurements of the optical and electronic properties of such arrays are needed to fully understand the implications of top-bottom anisotropy on their collective behavior, and specifically, the origin of the built-in voltage. However, the corresponding change in collective electronic properties along the growth direction can provide an explanation for a built-in electric field along the tube axis that enables THz generation by photocurrent excitation. For example, it has been established that in random arrays of mixed semiconducting and metallic SWCNTs, crossings between metallic and semiconducting nanotubes result in the

formation of Schottky barriers.<sup>34,35</sup> Significant disorder in SWCNT orientation on one side of the aligned array, as seen in Figure 1d, likely leads to the formation of more Schottky barriers close to the disordered edge. The associated contact electric field at the intersections of semiconducting and metallic SWCNTs then leads to drift photocurrents in semiconducting nanotubes upon optical excitation, similarly to what has been observed in GaAs nanowires that form Schottky barriers with Au caps.<sup>23</sup> An alternative mechanism is thermoelectric in nature and also relies on top-bottom asymmetry of SWCNT arrays. Differences in pump absorption between the top and bottom ends of the SWCNTs leads to a temperature gradient along the SWCNTs, resulting in predominantly unidirectional transient diffusive flow of hot carriers from the highly aligned array at the top end to the disordered region at the bottom end. It is worth noting that THz generation was not observed under the same excitation conditions in an aligned film of SWCNTs grown by the HiPco method, where the top and bottom sides of the nanotubes were random, underscoring the importance of top-bottom anisotropy of aligned SWCNT arrays for THz generation.

Another possible mechanism for THz generation is optical rectification, a  $\chi^{(2)}$  process that occurs in noncentrosymmetric, optical materials. While a large third-order nonlinear optical susceptibility,  $\chi^{(3)}$ , has been theoretically predicted for SWCNTs and measured using third-harmonic generation to be  $5.53 \times 10^{-12}$  esu for an aligned SWCNT film identical to the one used here,<sup>36</sup> no  $\chi^{(2)}$  processes such as second harmonic generation have been convincingly observed for SWCNTs. This

suggests that optical rectification is unlikely to contribute to THz generation in SWCNTs.

Both 400 and 800 nm optical pulses give rise to emission of THz radiation from the SWCNT film; however, as shown in Figure 3, excitation with 400 nm pulses appears to be more

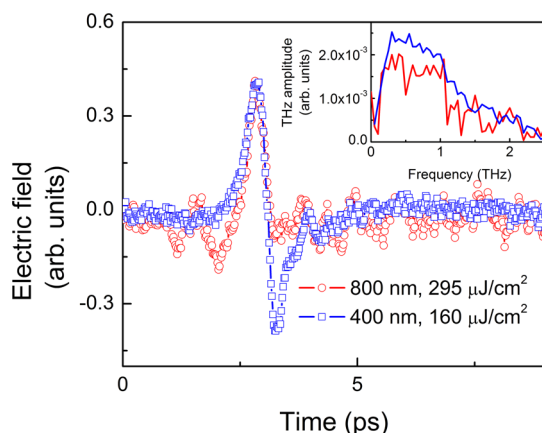


**Figure 3.** THz generation in the aligned SWCNT film: dependence on the pump pulse wavelength. Blue squares, 400 nm,  $160 \mu\text{J}/\text{cm}^2$  of absorbed fluence; red circles, 800 nm,  $295 \mu\text{J}/\text{cm}^2$ . Inset: corresponding amplitude spectra.

efficient, which may be explained by generation of multiple electron–hole pairs by 400 nm excitation. In Figure 3, the absorbed fluence is almost two times higher for the 800 nm beam, and the corresponding number of absorbed photons is almost four times higher; however, the peak THz electric field is the same, and THz power generated by 400 nm is higher (Figure 3, inset). Generation of multiple electron–hole pairs has been previously reported in semiconducting SWCNTs when the excitation energy is larger than the  $E_{22}$  transition energy.<sup>37,38</sup> With the average nanotube diameter being  $\sim 2.7$  nm in our sample, both 800 and 400 nm pump pulses have energy well above the  $E_{22}$  transition, but 400 nm pulses would be more likely to excite multiple electron–hole pairs per absorbed photon.<sup>39</sup> We also notice that excitation with 400 nm pulses produces bipolar THz waveforms, while excitation with 800 nm pulses does not. The reason for this is not presently clear, but the change from a half-cycle to a full-cycle THz transient for different pump wavelengths may provide insight into the mechanism of THz generation.

The effect of the absorbed optical pump fluence on the generated THz waveforms for  $\theta_{\text{pump}} = 90^\circ$  and  $\theta_{\text{SWCNT}} = 0^\circ$  is summarized in Figure 4 for 400 nm excitation (also in Figure S4 for 800 nm excitation). The absorbed pump fluence was determined by subtracting the transmitted and reflected fluence from the incident value. With increasing pump pulse fluence, the amplitude of the generated THz pulse increases (Figures 4a and S4a), while the spectral bandwidth remains unchanged, that is, 0.2–2.0 THz for 400 nm excitation (Figure 4b and Figure S5) and 0.1–1.5 THz for 800 nm excitation (Figure S4b). In both cases, the integrated THz amplitude, defined as the integral of the THz amplitude from 0–2.5 THz, saturates as the absorbed fluence is increased, as can be seen in Figure 4c for 400 nm excitation and in Figure S4c for 800 nm. Saturation of the emitted THz signal from biased photoconductive sources arises from screening of the bias voltage by photogenerated charge carriers<sup>40–42</sup> and can be described by a simple saturation function  $A_{\text{THz}} = BF/(F + S)$ , where  $B$  is a constant scaling factor,

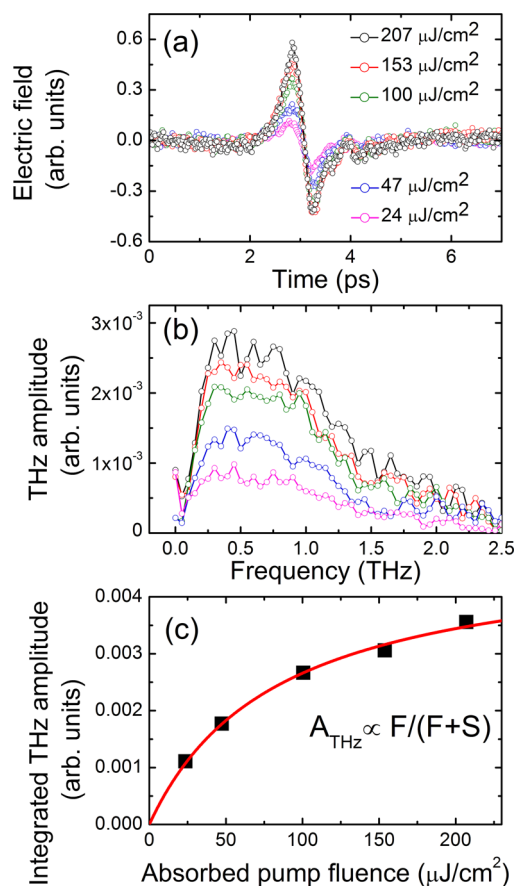


**Figure 4.** THz generation in the aligned SWCNT film: dependence on absorbed optical pump fluence. (a) THz pulse waveforms emitted after excitation with 400 nm pump pulses with absorbed fluence ranging from  $24$ – $207 \mu\text{J}/\text{cm}^2$ . (b) Corresponding THz amplitude spectra. (c) Integrated THz amplitude,  $A_{\text{THz}}$ , as a function of absorbed pump fluence,  $F$ , determined as an integral of the THz amplitude spectra in panel b from 0–2.5 THz. Symbols, experimental data; line, a fit to a saturation function.

$F$  is the absorbed pump fluence, and  $S$  is the saturation fluence.<sup>40,41</sup> In the fit shown in Figure 4c, the saturation fluence is found to be  $83 \pm 8 \mu\text{J}/\text{cm}^2$ , while a similar fit for 800 nm excitation (Figure S4c) yields a significantly higher saturation fluence of  $277 \pm 100 \mu\text{J}/\text{cm}^2$ .

Finally, Figure 5 explores the pump polarization dependence of the emitted THz power, where maximum THz power is achieved when the optical pump is polarized perpendicular to the SWCNT alignment direction. Similar behavior is seen for 800 nm pump. This seemingly counterintuitive phenomenon is caused by three factors: (1) significant anisotropy of optical absorption and reflectance of the aligned SWCNT films,<sup>10,43</sup> (2) sublinear (i.e., saturating) dependence of the generated THz amplitude on the pump pulse fluence, and (3) strong reabsorption of the emitted THz radiation by the aligned SWCNT film acting as a THz polarizer.<sup>9</sup> While the SWCNT film strongly absorbs pump pulses of all polarizations, absorbance as well as reflectance is higher for pump pulses polarized along the SWCNTs. At 400 nm, about 2% of incident light that is polarized along SWCNTs is reflected, and only 0.6% is transmitted through the  $2\text{-}\mu\text{m}$ -thick film. For 400 nm pump pulses polarized perpendicularly, the reflection loss reduces to  $\sim 0.8\%$ , but the transmission is increased by ten times to 6%, as shown in Figure S6. For 800 nm pump pulses,

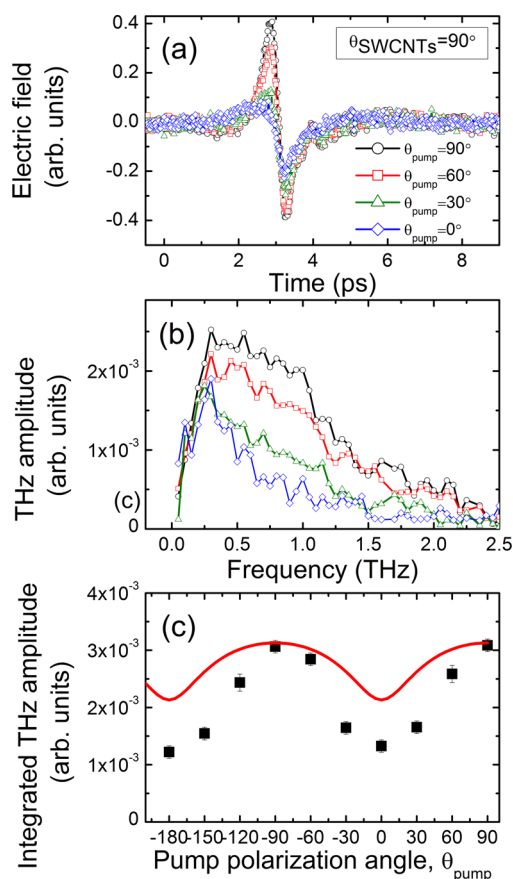


**Figure 5.** THz generation in the aligned SWCNT film: dependence on optical pump polarization. (a) THz pulse waveforms emitted after excitation with 400 nm pulses with pump polarization ranging from 0–90° (absorbed fluence is 160  $\mu\text{J}/\text{cm}^2$ ). (b) Corresponding THz amplitude spectra. (c) Integrated emitted THz amplitude, determined as an integral of the THz amplitude spectrum from 0–2.5 THz. Symbols, experimental data; line, a numerically evaluated integral of eq 1 with parameters  $S' = 0.027 \pm 0.002 \mu\text{J}/(\text{cm}^2 \text{nm})$  and  $B' = (6.04 \pm 0.05) \times 10^{-6}$  determined from a best fit to the data in Figure 4, panel c.

the anisotropy is even stronger, with the fraction of incident pump fluence that is transmitted through the film changing from 0.9% for parallel polarization to 12% for perpendicular polarization and reflection losses of  $\sim 3\%$  for parallel polarization and  $\sim 1.6\%$  for perpendicular polarization.

By using the experimentally determined reflectance and transmittance of the SWCNT film as a function of pump polarization, we calculate the polarization-dependent optical absorbance of this film,  $\alpha(\theta_{\text{pump}})$  and express, using the saturation function to model the generated THz amplitude, the integrated THz intensity generated at depth  $x$  from the front surface of the film, and emitted from the film's back surface, as

$$dA_{\text{THz, emitted}}(\theta_{\text{pump}}, x) = B' \frac{F'_{\text{abs}}(\theta_{\text{pump}})}{F'_{\text{abs}}(\theta_{\text{pump}}) + S'} \exp(-\alpha_{\text{THz}}(d-x)) dx \quad (1)$$

where  $F'_{\text{abs}}(\theta_{\text{pump}})$  is the pump fluence absorbed in  $dx$ , and  $S'$  and  $B'$  are the saturation fluence and a scaling constant per nanometer of film thickness, respectively, related to their whole-film counterparts  $S$  and  $B$  (Figure 4c). The exponential term takes into account significant reabsorption of THz

radiation in the film, where the THz absorption coefficient of the aligned SWCNT film at 0.6 THz was taken as  $\alpha_{\text{THz}} = 9655 \text{ cm}^{-1}$ , determined by measuring reflectance and transmittance of the film using a THz time-domain spectroscopy system (Advantest).<sup>9</sup> The parameters  $S'$  and  $B'$  were determined to be  $S' = 0.027 \pm 0.002 \mu\text{J}/(\text{cm}^2 \text{nm})$  and  $B' = (6.04 \pm 0.05) \times 10^{-6}$  by requiring the numerically integrated value of the total emitted THz amplitude at pump polarization  $\theta_{\text{pump}} = 90^\circ$  and at varying incident pump fluence to agree with the best fit of the fluence dependent integrated THz amplitude to the saturation function in Figure 4c. In this picture, absorption of the pump beam is much more uniformly spread across the thickness of the film for the pump pulses polarized normal to the SWCNTs, resulting in a higher overall THz generation over the entire film, and in more THz radiation generated closer to the back surface of the film and thus suffering from less reabsorption (Figure S7). Numerically integrating eq 1 for fixed excitation fluence (170  $\mu\text{J}/\text{cm}^2$ ) and a varying pump polarization, we get good qualitative agreement with the experimental data (Figure 5c). For a better quantitative agreement, we would likely need to allow for a variation in  $B'$  or  $S'$  with pump polarization.

For a fixed pump fluence and polarization, the emitted THz power is determined by the SWCNT film absorption coefficients in the visible and THz ranges as well as by the film thickness,  $d$ . By using eq 1, it is also possible to find an optimal film thickness for THz generation for a fixed set of absorption coefficients. We find this optimal thickness to be 1.5  $\mu\text{m}$ , which would lead to a  $\sim 5\%$  increase in emitted THz amplitude compared to a 2.0  $\mu\text{m}$  film (Figure S8).

In summary, we have observed generation of broadband (0.2–2.0 THz) THz pulses in a macroscopic film consisting of arrays of highly aligned SWCNTs. THz pulses are generated by photoexcitation of the aligned SWCNT arrays with either 400 or 800 nm pulses without any applied voltage bias. We also find that the generation efficiency is considerably higher for 400 nm excitation. Since the THz pulse is polarized parallel to the CNTs and has a polarity that reverses upon rotation of the film by 180°, we suggest that THz emission results from a photocurrent surge in SWCNTs due to a built-in electric field along the nanotube axis. The origin of this built-in field is likely related to the morphological difference between the tops and bottoms of the SWCNTs, with one end having dense, highly aligned SWCNTs and the other end characterized by less dense, disordered SWCNTs with a slightly larger average diameter. In the future, detailed spatially resolved measurements of the optical and electronic properties of such arrays will need to be carried out to conclusively identify the source of the built-in electric field responsible for the THz generation. By using the experimentally determined dependence of the integrated amplitude of the emitted THz pulse on the excitation fluence and polarization, we find that the optimal thickness of a highly aligned SWCNT film with built-in top-bottom anisotropy is  $\sim 1.5 \mu\text{m}$ . These results demonstrate that aligned SWCNT films have diverse and important applications in THz photonics; in addition to a THz polarizer<sup>9</sup> and powerless detector,<sup>8</sup> such aligned SWCNTs also have potential as active elements in THz sources.

## ■ ASSOCIATED CONTENT

### Supporting Information

Information on the SWCNT-generated THz power spectrum and estimated energy conversion efficiency, data ruling out

THz generation in the sapphire substrate, additional THz spectra recorded with 800 nm excitation for different samples orientations, dependence of THz generation in the aligned SWCNT film on absorbed optical pump fluence for 800 nm excitation, as well as normalized THz amplitude spectra for 400 nm excitation and transmission and reflectance of SWCNT films as a function of pump polarization for both 400 and 800 nm excitation. Additional details of the simulation of THz generation and emission for varying pump polarization and SWCNT film thickness. This material is available free of charge via the Internet at <http://pubs.acs.org>.

## AUTHOR INFORMATION

### Notes

The authors declare no competing financial interest.

## ACKNOWLEDGMENTS

L.V.T. and F.A.H. acknowledge funding from the Natural Sciences and Engineering Research Council of Canada (NSERC), Canada Foundation for Innovation (CFI), Alberta Science and Research Investment Program (ASRIP), Alberta Innovates Technology Futures (AITF), and the iCORE Centre for Interdisciplinary Nanoscience (iCiNano), and thank G. Popowich and D. Mullin for technical support. Q.Z. and J.K. were supported by DOE BES DE-FG02-06ER46308 (terahertz characterization of aligned carbon nanotubes) and the Robert A. Welch Foundation Grant No. C-1509 (sample preparation).

## REFERENCES

- (1) *Carbon Nanotubes: Synthesis, Structure, Properties, and Applications*; Dresselhaus, M. S., Dresselhaus, G., Avouris, P., Eds.; Springer-Verlag: Berlin, Germany, 2001.
- (2) Avouris, P.; Freitag, M.; Perebeinos, V. *Nat. Photonics* **2008**, *2*, 341–350.
- (3) Bonaccorso, F.; Sun, Z.; Hasan, T.; Ferrari, A. C. *Nat. Photonics* **2010**, *4*, 611–622.
- (4) Nanot, S.; Hároz, E. H.; Kim, J.-H.; Hauge, R. H.; Kono, J. *J. Adv. Mater.* **2012**, *24*, 4977–4994.
- (5) Beard, M.; Blackburn, J. L.; Heben, M. J. *Nano Lett.* **2008**, *8*, 4238.
- (6) Jensen, S. A.; et al. *Nano Lett.* **2013**, *12*, 5925.
- (7) Hartmann, R. R.; Kono, J.; Portnoi, M. E. *Nanotechnology* **2014**, *25*, 322001.
- (8) He, X.; et al. *Nano Lett.* **2014**, *14*, 3953–3958.
- (9) Ren, L.; et al. *Nano Lett.* **2012**, *12*, 787–790.
- (10) Docherty, C. J.; et al. *J. Appl. Phys.* **2014**, *115*, 203108.
- (11) Bahk, Y.-M.; et al. *ACS Nano* **2014**, *8*, 9089–9096.
- (12) Kibis, O. V.; Portnoi, M. E.; da Costa, M. R. *Nano Lett.* **2007**, *7*, 3414–3417.
- (13) Portnoi, M. E.; Kibis, O. V.; da Costa, M. R. *Superlattices Microstruct.* **2008**, *43*, 399–407.
- (14) Mittleman, D. M. *Nat. Photonics* **2013**, *7*, 666.
- (15) Jepsen, P. U.; Cooke, D. G.; Koch, M. *Laser Photonics Rev.* **2011**, *5*, 124.
- (16) Baxter, J. B.; Guglietta, G. W. *Anal. Chem.* **2011**, *83*, 4342.
- (17) Schneider, A.; et al. *J. Opt. Soc. Am. B* **2006**, *23*, 1822.
- (18) Stepanov, A. G.; et al. *Opt. Mater. Express* **2014**, *4*, 870.
- (19) Nahata, A.; Auston, D. H.; Wu, C.; Yardley, J. T. *Appl. Phys. Lett.* **1995**, *67*, 1358–1360.
- (20) Johnston, M. B.; Whittaker, D. M.; Corchia, A.; Davies, A. G.; Linfield, E. H. *Phys. Rev. B* **2002**, *65*, 165301.
- (21) Malevich, V. L.; Adomavičius, R.; Krotkus, A. C. *R. Physique* **2008**, *9*, 130–141.
- (22) Takahashi, K.; et al. *Adv. Optical Mater.* **2014**, *2*, 248.
- (23) Trukhin, V. N.; et al. *Appl. Phys. Lett.* **2013**, *103*, 072108.
- (24) Ahn, H.; et al. *Appl. Phys. Lett.* **2007**, *91*, 132108.
- (25) Jung, G. B.; et al. *Opt. Express* **2010**, *18*, 16353.
- (26) Lee, W.-J.; et al. *Sci. Rep.* **2013**, *3*, 1984.
- (27) Ramakrishnan, G.; Chakkittakandy, R.; Planken, P. C. M. *Opt. Express* **2009**, *17*, 16092.
- (28) Pint, C. L. *J. Nanosci. Nanotechnol.* **2008**, *8*, 6158.
- (29) Pint, C. L.; et al. *Nano Lett.* **2008**, *8*, 1879.
- (30) Amama, P. B.; et al. *Nano Lett.* **2009**, *9*, 44–49.
- (31) Pint, C. L. *ACS Nano* **2010**, *4*, 1131–1145.
- (32) Ren, L.; et al. *Phys. Rev. B* **2013**, *87*, 161401(R).
- (33) Titova, L. V.; et al. *Phys. Rev. B* **2011**, *83*, 085403.
- (34) Topinka, M. A.; et al. *Nano Lett.* **2009**, *9*, 1866.
- (35) Stadermann, M.; et al. *Phys. Rev. B* **2004**, *69*, 201402(R).
- (36) Morris, D. T.; et al. *Phys. Rev. B* **2013**, *87*, 161405(R).
- (37) Gabor, N. M.; Zhing, Z.; Bosnick, K.; Park, J.; McEuen, P. L. *Science* **2009**, *235*, 1367.
- (38) Wang, S.; Khafizov, M.; Tu, X.; Zheng, M.; Krauss, T. D. *Nano Lett.* **2010**, *10*, 2381.
- (39) Weisman, R. B.; Bachilo, S. M. *Nano Lett.* **2003**, *3*, 1235.
- (40) Reid, M.; Fedosejevs, R. *Appl. Opt.* **2005**, *44*, 149.
- (41) Ropagnol, X.; Blanchard, F.; Ozaki, T.; Reid, M. *Appl. Phys. Lett.* **2013**, *103*, 161108.
- (42) Castro-Camus, E.; Lloyd-Hughes, J.; Johnston, M. B. *Phys. Rev. B* **2005**, *71*, 195301.
- (43) Murakami, Y.; Einarsson, E.; Edamura, T.; Maruyama, S. *Phys. Rev. Lett.* **2005**, *94*, 087402.